

## The Solar Line Emission Dopplerometer project

Jean-Marie Malherbe · Pierre Mein · Frédéric  
Sayède · Pawel Rudawy · Kenneth Phillips ·  
Francis Keenan · Jan Rybák

Received: 2 April 2021 / Accepted: date

**Abstract** Observations of the dynamics of solar coronal structures are necessary to investigate space weather phenomena and global heating of the corona. The profiles of high temperature lines emitted by the hot plasma are usually integrated by narrow band filters or recorded by classical spectroscopy. We present in this paper details of a new transportable instrument (under construction) for imaging spectroscopy: the Solar Line Emission Dopplerometer (SLED). It uses the Multi-channel Subtractive Double Pass (MSDP) technique, which combines the advantages of both filters and narrow slit spectrographs, i.e. high temporal, spatial and spectral resolutions. The SLED will measure at high cadence (1 Hz) the line-of-sight velocities (Doppler

---

J.-M. Malherbe  
LESIA, Observatoire de Paris, PSL Research University, CNRS, 92195 Meudon, France  
E-mail: jean-marie.malherbe@obspm.fr

P. Mein  
LESIA, Observatoire de Paris, PSL Research University, CNRS, 92195 Meudon, France  
E-mail: pierre.mein@club-internet.fr

F. Sayède  
GEPI, Observatoire de Paris, PSL Research University, CNRS, 92195 Meudon, France  
E-mail: frederic.sayede@obspm.fr

P. Rudawy  
Astronomical Institute, University of Wrocław, Poland  
E-mail: rudawy@astro.uni.wroc.pl

K.J.H. Phillips  
Earth Sciences Department, Natural History Museum, London SW75BD, United Kingdom  
E-mail: kennethjhphillips@yahoo.com

F.P. Keenan  
Astrophysics Research Centre, School of Mathematics and Physics, Queen's University Belfast, United Kingdom  
E-mail: f.keenan@qub.ac.uk

J. Rybák  
Astronomical Institute, Slovak Academy of Sciences, 05960 Tatranská Lomnica, Slovakia  
E-mail: rybak@astro.sk

shifts) of hot coronal loops, in the forbidden lines of FeX 6374 Å and FeXIV 5303 Å. It will follow the dynamics of fast evolving events of solar activity such as flares or Coronal Mass Ejections (CMEs), and also study coronal heating by short period waves. Observations will be performed with the coronagraph at the Lomnický Štít Observatory (LSO, in Slovakia) or during total eclipses. The SLED will also observe the dynamics of solar prominences in H $\alpha$  6563 Å or He D3 5876 Å lines when mounted on the Białków coronagraph (near Wrocław, Poland). It is fully compatible with polarimetric measurements by various techniques.

**Keywords** Sun – Instrumentation – Imaging spectroscopy – Prominences – Corona – Dynamics –

## 1 Introduction

Solar activity is the primary driver of space weather (e.g., Schrijver et al., 2012; Pomoell and Poedts, 2018). It occurs over timescales ranging from seconds to several minutes in solar flares and CMEs (Shibata and Magara, 2011), which are fast evolving events and highly dynamic phenomena, originating in the solar atmosphere from non-potential energy stored in magnetic fields. Observational data for coronal loops, and their main properties and models, are reviewed by Reale (2010).

The hot corona has been imaged in the extreme ultraviolet (EUV) at 45 s cadence by the Atmospheric Imaging Assembly onboard Solar Dynamics Observatory (SDO/AIA) since 2010 in many wavebands containing highly ionized lines of iron (171, 193, 211, 335, 94, 131 Å respectively for temperatures of 0.6, 1.0, 2.0, 2.5, 6.0 and 10.0 MK). STEREO, since 2006, uses similar wavebands (171, 195, 284 Å) plus two coronagraphs. The Solar and Heliospheric Observatory (SOHO), launched in 1995, is still active in these wavebands (EIT telescope) and with the C2/C3 wide field and white light coronagraphs of LASCO. Solar Orbiter, launched in 2020, will soon offer, with the EUI instrument (Rochus et al., 2020), coronal images in wavebands at 171 and 335 Å. In parallel, high altitude coronagraphs allow observations at much higher cadence (sub-second), such as the SECIS instrument (Phillips et al. (2000), Ambróz et al. (2010)) working in white light and in the green coronal line of FeXIV 5303 Å.

The corona is also observed during total solar eclipses in several high temperature emission lines including FeX 6374 Å (red line) and FeXIV 5303 Å (green line), as well as in infrared (IR) lines such as FeXI 7892 Å (Habbal et al. (2011), Boe et al. (2018), Rudawy et al. (2019)).

However, none of the above imaging instruments can measure the plasma velocities in the corona. Various instrumental techniques, such as radar echoes, have been used in the past to probe the solar corona and measure Doppler shifts. For example, Chisholm and James (1964) found frequency shifts in 38.25 MHz radar signals reflected by the corona. James (1970) suggested that such echoes could be due to compressional waves related to coronal heating or to mass motions with velocities less than 50 km s<sup>-1</sup>. Desai et al. (1982) carried out Fabry-Pérot interferometric observations of the coronal FeXIV green line and confirmed mass motions in the 30-50 km s<sup>-1</sup> range. LASCO/C1, onboard SOHO, was operational from 1995 to 1998 and

able to scan the green (FeXIV) and red (FeX) lines with a Fabry-Pérot tunable filter (respectively 0.65 and 0.85 Å spectral resolution, Brueckner et al. (1995)). Mierla (PhD Thesis, Göttingen, 2005) and Mierla et al. (2008) reported velocities of the order of  $10 \text{ km s}^{-1}$  in the quiet corona, but C1 was not able to measure velocities for short duration dynamic events such as CMEs, due to the long time needed (15 minutes) to scan the line profiles. Among ground-based coronagraphs, the Coronal Multi-channel Polarimeter (CoMP, Tomczyk et al. (2008)) is a tunable birefringent filter and full Stokes polarimeter working in the IR lines of FeXIII 10747 Å and 10748 Å (1.3 Å FWHM). CoMP is able to measure line-of-sight (LOS) velocities and magnetic fields, with temporal resolution of about 15 s and spatial scale of 4.35". Morton et al. (2016) used CoMP to identify transverse-like waves that peaked at frequencies of around 3 mHz.

In spectroscopy, multi-slit spectra of the green line have been reported by Livingston et al. (1980) and Livingston and Harvey (1982). Singh et al. (2002) have investigated the properties of the coronal FeXIV and FeX emission lines, using slit spectroscopy at high spectral resolution (respectively 0.03 and 0.06 Å). Spectra of the FeXIV line (0.02 Å resolution) were also recorded by Sakurai et al. (2002). Minarovjech et al. (2003) reported the detection of oscillations in the green line observed at LSO and at Norikura (nearly simultaneously) using slit spectroscopy. Lee et al. (2021) combined simultaneous Doppler measurements from CoMP (FeXIII 10747 Å) and EIS onboard Hinode (FeXII 195 Å, FeXIII 202 Å) and found a good correlation above active regions.

The SLED instrument described in this paper will provide an unique opportunity to measure plasma velocities in the coronal green and red lines at high cadence (1 Hz), by combining the advantages of both spectroscopy and tunable filters. Our paper is organized as follows. Section 2 summarizes the principles and history of the imaging spectroscopy concept used by the SLED in a state-of-the-art manner, while Section 3 presents the main scientific goals of the SLED. The capabilities of the new instrument are described in Section 4, while Section 5 provides details concerning the optical design.

## 2 The Multichannel Subtractive Double Pass (MSDP)

The SLED is a promising, highly optimized and compact version of the MSDP spectrograph; the principle behind the instrument is illustrated in Figure 1. The MSDP was first described by Mein (1977), and has been upgraded many times over the last four decades on several telescopes in Europe (Meudon Solar Tower, Pic du Midi Turret Dome, Vacuum Tower Telescope and THEMIS at Tenerife, Białków coronagraph; see Mein et al. (2021)).

It is an imaging double pass spectrograph using a 2D rectangular entrance window (F1) and a slicer (S). In the spectrum (F2), after a first pass on the grating (R), the slicer has two functions: it selects N channels (beam-splitting) and realigns the N channels (beam-shifting) before the subtraction of the dispersion by the second pass on the grating. The beam-splitter can be either slit or micro-mirror based, while the beam-shifter uses either prisms or mirrors. Output of the MSDP is composed

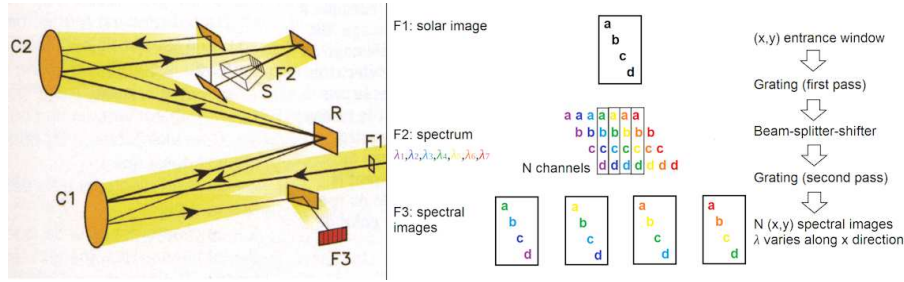


**Fig. 1** The principle of the MSDP spectroscopy. Left: the spectrograph; F1 = entrance window; C1 = collimator; C2 = chamber objective; R = grating; F2 = spectrum; S = slicer (beam-splitter, beam-shifter); F3 = multichannel spectra image and camera. Right: the three successive steps of a schematic MSDP with  $N = 4$  channels; top = solar image at entrance window F1; middle = slicer S in the spectrum at F2 (first pass, the colours of the letters correspond to the light dispersion); bottom:  $N = 4$  spectra images at F3 (after second subtractive pass), with varying wavelength along the x-direction).

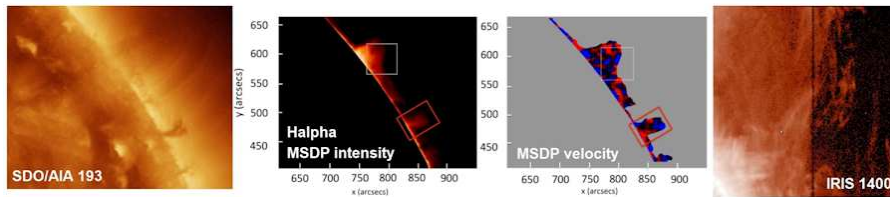


**Fig. 2** Typical coordinated observations (24 September 2013 at 12:22 UT) with SDO/AIA (193 Å, left), the Meudon MSDP (H $\alpha$  intensity and Doppler velocity) and IRIS (slit jaw at 1400 Å, right). The white rectangle (prominence) delineates the IRIS FOV (50''  $\times$  50''), while the red box indicates the tornado.

of  $N$  contiguous spectra-images ( $N$  increased from 7 to 24 during four decades of advances). There is a constant wavelength step between each spectra-image, but inside each, the wavelength varies linearly along the x-direction. This technique allows the derivation of data cubes ( $x$ ,  $y$ ,  $\lambda$ ), where the three coordinates are simultaneous while extracted from a single exposure. Hence, the MSDP combines the advantages of imaging filters and spectroscopy, and the spatial resolution is identical to that provided by filters. The FOV depends on the focal length of the telescope and the size of the window (F1); the size can be as large as 60'' in the x-direction and 500'' in the y-direction. Spectral resolution is in the range 0.03 - 0.3 Å (according to the focal length of the spectrograph and the slicer technology), while the cadence may reach several frames/s, depending on the photon flux.

Figure 2 shows typical processed observational data of prominences and tornadoes which have been performed with the MSDP in coordination with space-borne instruments such as IRIS (Schmieder et al., 2014).

The MSDP is fully compatible with polarimetric observations. Many techniques have been used on various telescopes: Stokes V with liquid crystals at Meudon (Figure 3) and Pic du Midi (Roudier et al., 2006); static birefringent plates at THEMIS for Stokes Q, U, V. The polarimeter is installed in the image plane near the entrance window F1 of Figure 1.

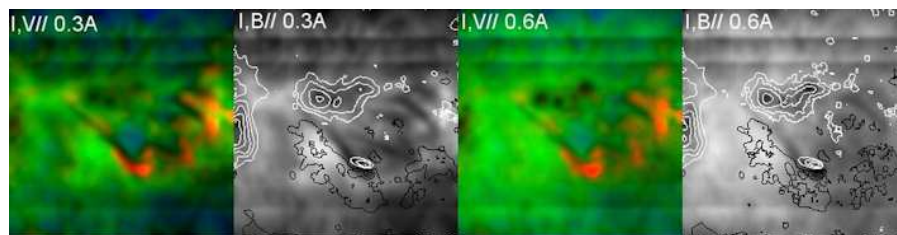


**Fig. 3** Polarimetric test on an active region with the Meudon MSDP. Intensity  $I$ , LOS velocity  $V//$ , and line of sight magnetic field  $B//$  at two positions in the  $H\alpha$  line ( $0.3 \text{ \AA}$  and  $0.6 \text{ \AA}$  chords above line centre) corresponding to two different altitudes.  $B//$  is represented by contours (white/black for North/South polarities).  $V//$  is colour-coded (blue/red shifts). FOV  $300'' \times 300''$ .

### 3 The scientific objectives of the SLED

The SLED has two main goals which can be achieved owing to its capability to produce Dopplergrams for the whole FOV at high cadence (1 Hz).

#### 3.1 Highly dynamic events

SLED will observe the dynamics of coronal loops in active regions, flares and CMEs, driving solar-terrestrial interactions and space weather events. Crucially, it will provide a new diagnostic via plasma velocity measurements (Doppler shifts) inside hot loops at high temporal resolution. This outstanding feature can be combined with data obtained by AIA onboard SDO (intensity of several lines between 0.6 MK and 10 MK at lower cadence). SLED, with its LOS velocity measurements, will impose new constraints on models of hot coronal loops and their time evolution. While line intensity information allows us to visualize qualitatively plasma motions in the plane of the sky, Doppler shifts provide a direct determination of the LOS velocity. SLED will be operational well before the forthcoming solar maximum of cycle 25 (predicted in 2025) and will measure velocities for highly dynamic events which play a major role in space weather.

#### 3.2 Coronal heating

The SLED will search for high-frequency, wave-like variations in the plasma velocities over small spatial scales in the solar corona, particularly in loops associated with active regions. It allows quantitative studies of wave processes contributing to the plasma heating, energy balance of the corona and tests of coronal heating models. SLED will not search for intensity fluctuations but for motions derived from Doppler shifts in the green and red forbidden lines, as seen by Tomczyk et al. (2007) in the near-infrared FeXIII lines.

The physical process involved in the heating of the solar corona is not yet definitively identified (Klimchuk, 2006). The main mechanisms that have been studied fall

into two categories: heating by numerous small magnetic reconnection events (nanoflares) or by the dissipation of Alfvén or magnetohydrodynamic (MHD) waves in coronal loops.

Observations with CoMP at Sacramento Peak (Tomczyk et al., 2007) have shown evidence for Alfvén-type wave motions around active regions at the limb. The waves were upward-propagating with low frequencies (3.5 mHz). However, the total energy flux of these waves is insufficient for the coronal heating. The investigation of much higher-frequency waves (1 Hz) is not possible with current space missions owing to telemetry limitations, and therefore has been undertaken during total solar eclipses with ground-based instruments. In these studies, the corona has been imaged using narrow-band filters (typically up to 5 Å) in the FeXIV green line or FeX red line with fast CCD cameras. Several observational campaigns were organized with the SECIS instrument (Phillips et al. (2000), Rudawy et al. (2004), Rudawy et al. (2010), Rudawy et al. (2019)), but a careful analysis showed that the short period intensity fluctuations are questionable in terms of waves. For this reason, the SLED will search instead for signatures of Doppler shifts in wave-like phenomena.

#### 4 The SLED capabilities

The core of the SLED is the 24 channels slicer. It is designed for F/30 beams and can be easily coupled to various existing telescopes. Hence, it is envisaged to become a permanent instrument for the large Białków coronagraph (prominence observations) or for the high-altitude LSO coronagraph (high temperature emission lines). It will also be used for total eclipse campaigns, as it is a portable spectrograph. In summary, the SLED can be mounted on the following telescopes with easy focal length adaptation:

- the 2.0 m focal length / 0.20 m aperture Celestron telescope at Wrocław (6.0 m equivalent focal length with Barlow 3.0 ×) and heliostat (or equatorial mount) for total eclipse campaigns, providing a 150'' × 1000'' FOV with 2.1'' pixel sampling.
- the 4.0 m focal length / 0.2 m aperture Zeiss coronagraph (Lexa, 1963) at LSO (6.0 m equivalent focal length with Barlow 1.5 ×), for coronal observations (hot plasma), 150'' × 1000'' FOV with 2.1'' pixel sampling.
- the 14.5 m focal length coronagraph (0.50 m aperture) at Białków observatory providing a 62.5'' × 450'' FOV with 0.9'' pixel sampling (possibly two times larger with 0.25 m diaphragm and focal length reduced to 7.25 m), for prominence observations (cold plasma).

Coronal lines will be observed at the LSO coronagraph or during total eclipses (the Barlow is the only element that will change). However, SLED can also observe in H $\alpha$  6563 Å or the He D3 5876 Å lines to study the dynamics of prominences with the Białków coronagraph. Indeed, the SLED would considerably improve the capabilities of the MSDP already operating there with only 9 channels.

The wavelength transmissions of the 24 channels in terms of Doppler shifts (converted to velocities, positive for blue shifts) are displayed in Figure 4 for the coronal green and red lines (LSO and eclipse telescopes, 6.0 m equivalent focal length) and

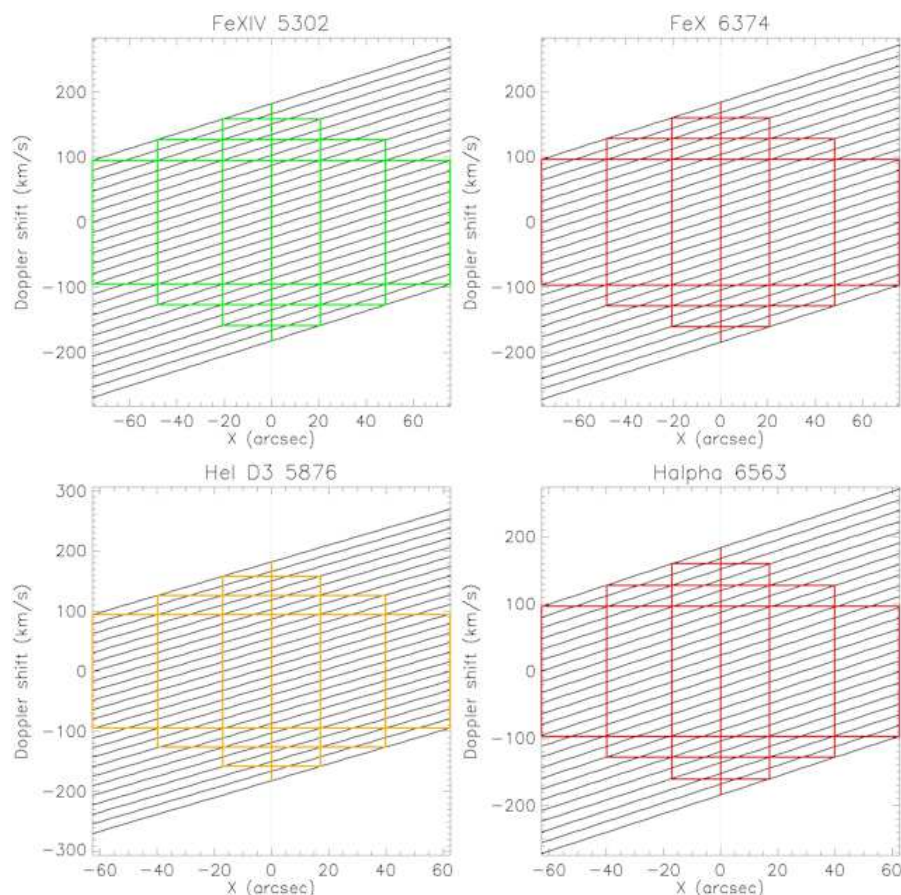


**Fig. 4** Wavelength functions of the 24 channels of the SLED. Abscissae: the x-direction ( $''$ ); ordinates: the wavelength variation converted to velocities ( $\text{km s}^{-1}$ ). Top: coronal lines (left: FeXIV, right: FeX) for LSO coronagraph or eclipses; bottom: prominence lines (left: He D3, right:  $H\alpha$ ) for Białków coronagraph.

for the prominence lines (Białków coronagraph, 7.25 m focal length). Note that the channels are not monochromatic; the wavelength varies linearly in the x-direction (along the width of the FOV). Figure 4 shows that large velocities can be determined everywhere in the full FOV. However, the three rectangular selections (in terms of x-direction and wavelength) show that there is a linear relationship between the highest measurable velocities and the FOV width. For the green line, the maximum Doppler shift (converted to velocity) is given by the relation  $|v_{max}| = -1.17|x| + 183 \text{ km s}^{-1}$  where  $x$  is the abscissa ( $''$ ) along the 2D FOV. Hence, the SLED is well adapted to the highly dynamic phenomena and the fast evolving events associated with solar activity.

Figure 5 shows a simulation of the 24 channels for the FeXIV green line, the profile of which is assumed to be Gaussian. The FWHM of the profile is  $0.8 \text{ \AA}$  (Singh et al., 2002) and the line is centred between channels 12-13 (top row). The middle and bot-

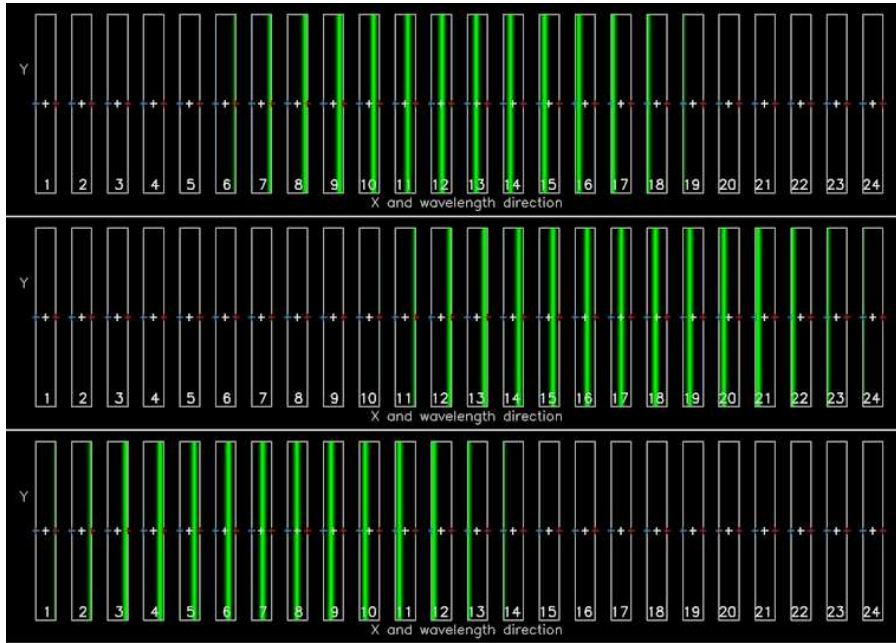
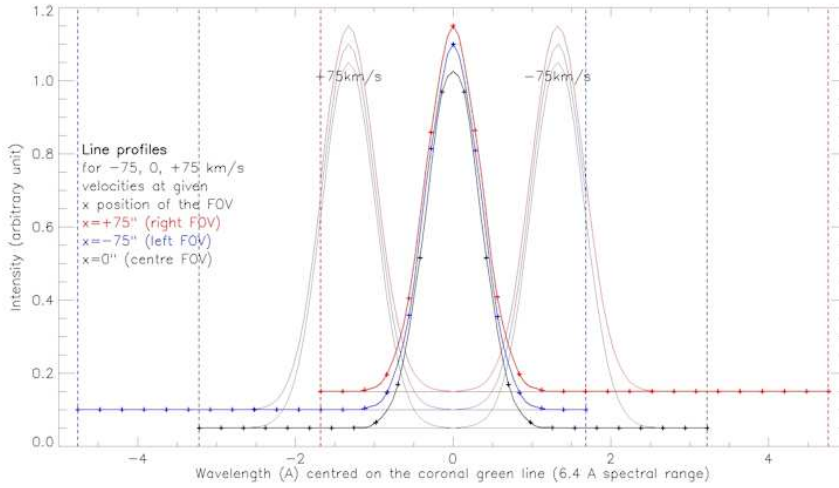


**Fig. 5** A simulation of spectra images of the FeXIV green line (no velocity, top) and with redshifts ( $-75 \text{ km s}^{-1}$ , middle) or blueshifts ( $+75 \text{ km s}^{-1}$ , bottom). The crosses refer to the three specific locations in the x-direction (left, centre, right of the FOV) indicated in Figure 6.

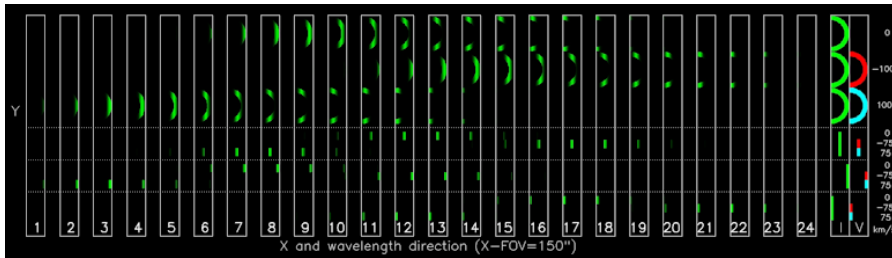
tom parts of Figure 5 show how the line is affected by LOS velocities of respectively  $-75 \text{ km s}^{-1}$  (red shift) and  $+75 \text{ km s}^{-1}$  (blue shift). Three points indicated by crosses (left, centre and right of the FOV in the x-direction) refer to the profiles of Figure 6. In the centre of the FOV, the spectral range provided by the 24 channels is  $[-3.25 \text{ \AA}, +3.25 \text{ \AA}]$ , allowing the measurement of Doppler shifts in the range  $[-2.85 \text{ \AA}, +2.85 \text{ \AA}]$  (to take into account the line width), corresponding to velocities up to  $160 \text{ km s}^{-1}$ . Towards the edges, the spectral domain has the same width ( $6.5 \text{ \AA}$ ) but is shifted:  $[-4.8 \text{ \AA}, +1.7 \text{ \AA}]$  or  $[-1.7 \text{ \AA}, +4.8 \text{ \AA}]$  respectively for the left and right sides; there velocities up to  $75 \text{ km s}^{-1}$  can still be determined. Steady flows in coronal loops exhibit velocities which are often smaller, but in the cases of ejected material, the SLED will be able to measure velocities not far from the sound speed ( $150 \text{ km s}^{-1}$ ).

Figure 7 shows another simulation of the 24 channels of the SLED corresponding to several models of structures displayed in the column I (intensity) and V (LOS velocity in  $\text{km s}^{-1}$ ), under the assumption of Gaussian line profiles ( $0.8 \text{ \AA}$  FWHM). In practice, the 24 channels are approximately parallelograms detected by the data processing algorithm and transformed into 24 rectangles of the same size, after correcting for geometrical distortions. Subsequently, the algorithm uses the information from the 24 channels of the spectra images to recover the line profiles and derive intensity and velocity maps, after correction by the flat field (observed generally at disk centre). The restoration of the line profiles is based on the transmission curves of Figure 4 and cubic interpolation between sampling points ( $0.28 \text{ \AA}$  step). As standard





**Fig. 6** Line profiles at the three locations selected in Figure 5, with LOS velocities of 0, -75 and +75 km s<sup>-1</sup>. Black: profiles at the centre of the FOV. Blue/red: profiles respectively at the left/right sides of the FOV. Crosses show the measurement points; a cubic interpolation is applied between them. The spectral range is 6.5 Å; it shifts from the left to the right sides of the FOV, so that the centering of the line varies in x-direction.



**Fig. 7** Simulation of the 24 channels of the SLED for a model of observations shown at right in the columns I (intensity) and V (velocity).

polynomial interpolations between them (0.07 Å step) generate errors, in particular in the line core, we propose a two-step method to restore as best as possible the profiles.

In Figure 8, we have plotted a theoretical Gaussian profile in black. This is then sampled by the slicer of the SLED (0.28 Å for both step and bandwidth) and the measurement points are indicated by black squares (A). The cubic interpolation between points A provides the red crosses (0.07 Å step). This "first-order" restored profile reveals errors, mainly in the vicinity of the line core. In order to compensate for these, we compute a "second-order" profile (blue signs, C points). For that purpose, the "first-order" profile is re-sampled similarly (0.28 Å step and bandwidth) providing the red triangles (B points). Then, we apply a correction such that AC = BA (thus BC = 2 BA), providing the "second-order" restored profile indicated by the blue signs (C). This two-step method provides restored profiles (the C points) which

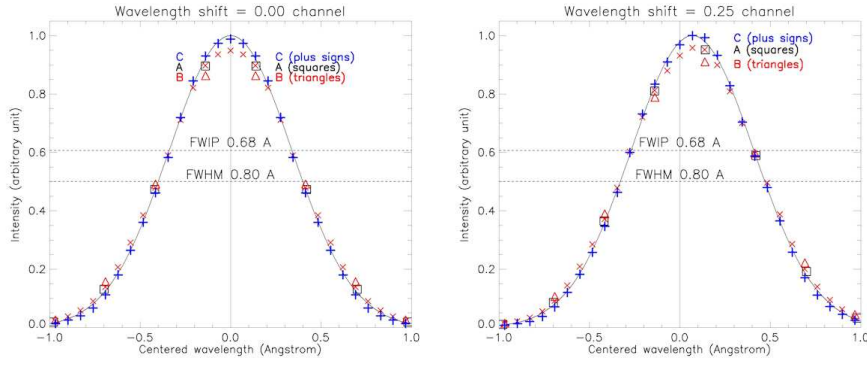


**Fig. 8** Improved interpolation method proposed for the SLED. Left and right pannels just differ by the distribution of sampling points (which depend on the pixel location in the x-direction and/or the Doppler shift; the right example has a shift of 1/4 channel = 0.07 Å). Solid (black) line: theoretical Gaussian profile. Black squares (A): sampling points by the slicer (0.28 Å step and bandwidth). Red crosses: cubic interpolation between sampling points ("first order" restored profile). Red triangles (B): sampling points of the "first order" profile (0.28 Å step and bandwidth). Blue signs (C): corrected positions (B → C, such that  $BC = 2 BA$ ) providing the "second order" restored line profile. FWIP = Full Width at Inflexion Points, FWHM = Full Width at Half Maximum.

are the most accurate above and below the inflexion points (respectively in the line core and wings).

LOS velocities are derived from the restored profiles using the bisector technique. For that purpose, we choose a chord of given width and compute the wavelength position of the middle of the chord. The simulation allows us to assess the precision of velocity measurements for different chords. Figure 9 shows that the best precision is always obtained with a chord of 0.70 Å between the inflexion points (because the slope is maximum there). For the FeXIV green line, assuming a gaussian shape, we found a FOV averaged error of  $\pm 0.05 \text{ km s}^{-1}$ ; locally, it may reach  $\pm 0.08 \text{ km s}^{-1}$  (depending on the location of the sampling points along profiles). Below or above the inflexion points, errors are higher ( $\pm 0.23 \text{ km s}^{-1}$ ).

It is well known from the signal-to-noise ratio (S/N) of observations that photon noise is an important source of error. In order to simulate this, we introduced a Poisson-type noise on line profiles and found a FOV averaged error of  $\pm 0.35$ ,  $\pm 0.18$ ,  $\pm 0.10$ ,  $\pm 0.06 \text{ km s}^{-1}$  for respectively  $S/N = 25, 50, 100, 200$  (Figure 10), in the case of velocity measurements at the inflexion points of the line. The sCMOS detector cannot exceed a S/N ratio of 150 for a single exposure (30000 electrons full well capacity), providing a typical velocity error of  $\pm 0.07 \text{ km s}^{-1}$ . Photon noise is negligible for S/N ratios above 200. For 1 Hz observing cadence we expect for the SLED the S/N ratio of 50, so that the sampling and cubic interpolation errors ( $\pm 0.05 \text{ km s}^{-1}$ ) will be dominated by the photon noise ( $\pm 0.18 \text{ km s}^{-1}$ ). At slower cadences (0.25 Hz or less), the restoration will just be limited by the interpolations.

The movie (see appendix) presents a simulation of the SLED channels for the coronal green and red lines emitted by artificial structures with varying velocities in the interval  $[-100 \text{ km s}^{-1}, +100 \text{ km s}^{-1}]$ , together with the associated line profiles.

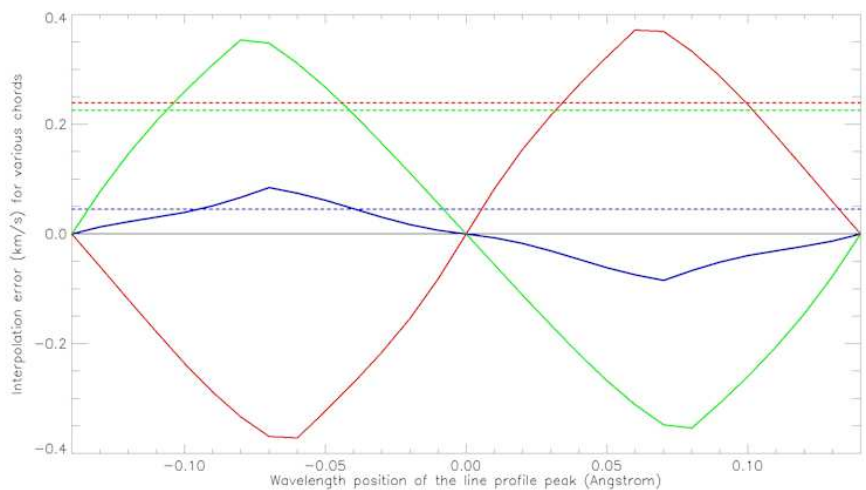


**Fig. 9** Velocity error for different chords as a function of the wavelength sampling of the line profile. The wavelength range (1 channel = 0.28 Å) is the period of the plot. For positions -0.14, 0, +0.14 Å, sampling points are symmetrical and the errors vanish. The chord widths are 0.70, 0.84 and 0.56 Å, respectively for blue, green and red solid lines. The corresponding RMS error levels (0.05, 0.22, 0.24 km s<sup>-1</sup> respectively) are indicated by the dashed lines.

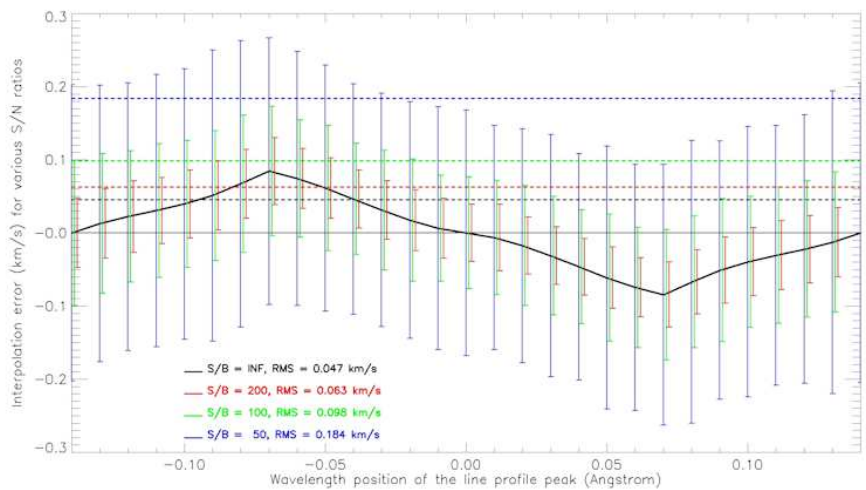


**Fig. 10** Influence of photon noise on the precision of velocity measurements as a function of the wavelength sampling of the line profile. The wavelength range (1 channel = 0.28 Å) is the period of the plot. The error bars indicate the effect of the photon noise for S/N = 50, 100, 200 (respectively blue, green and red bars). The corresponding RMS error levels (0.18, 0.10, 0.06 km s<sup>-1</sup> respectively) are indicated by the dashed lines.

As a future option, the SLED could operate in polarimetric mode for magnetic field strength and direction determination. Mein et al. (2021) describe a full Stokes polarimeter optimized for the MSDP imaging spectroscopy. It uses a calcite beam splitter which reduces the FOV in the x-direction by a factor two, and hence provides two simultaneous measurements (I+S, I-S with S = Stokes Q, U, V in sequence). In order to preserve the FOV in the x-direction, an alternative method is to measure sequentially I+S and I-S, as implemented by Roudier et al. (2006) at the MSDP of the Pic du Midi turret dome. The polarimeter takes place at the entrance window of the spectrograph and is based on Liquid Crystal Variable Retarders (LCVR) allowing fast observations. While one crystal is needed for Stokes Q and V, two are required for U. The signals delivered by the optional polarimeter would be:

$$\frac{1}{2}[I \pm (Q \cos \delta_2 + \sin \delta_2 (U \sin \delta_1 - V \cos \delta_1))] ]$$

where  $\delta_1$  and  $\delta_2$  are the two LCVR retardances.

## 5 The SLED optical design

The spectral resolution (0.28 - 0.34 Å) and coverage (6.5 Å) of the SLED is well adapted to coronal line widths (typically 0.8 Å) and large Doppler shifts ( $\pm 100 \text{ km s}^{-1} \approx \pm 2.0 \text{ Å}$ ), and its large FOV ( $150'' \times 1000''$ , 2.1'' spatial sampling) is compatible with the size of coronal structures ( $10^5 \text{ km}$  or more). We extrapolated from SECIS observations that the expected cadence (only limited by the photon flux of the 0.20 m aperture) is one frame/s for a S/N ratio of 50, and several frames/s if a smaller S/N ratio is acceptable (depending on the scientific program). The slicer is built by Paris observatory; the spectrograph design, prepared in Paris, will be assembled and tested by Wrocław to be fully operational well in advance of the next solar maximum in 2025. SLED will also be available for the total solar eclipse of 8 April 2024, visible from North America.

The transfer optics to the SLED is detailed by Figure 11, for the case of the LSO coronagraph (0.2 m diameter, 3.0 m primary focus, 4.0 m secondary focus). The post-focus instrument mechanical interface allows the inspection of the entire solar limb (TILT1 angle). SLED includes a field rotator (M1, M2, M3 mirrors) allowing us to explore the solar corona up to 0.8 solar radii above the limb. The 2D entrance window will be tangential to the limb, but can also be inclined (TILT2 angle) to fit better to the coronal loop's topology. The diverging doublet B provides a F/30 focus (6.0 m equivalent focal length). Red and green light beams are separated by the dichroic mirror D to form two solar images at the focus of the SLED spectrograph. In Figure 11, P are compensating plates (for accurate focusing of green and red lines) and FL are field lenses to reject the entrance pupil at large distances.

The optical path of the SLED spectrograph is given in Figure 12 for the FeX and FeXIV coronal lines. The letters L and M represent lenses and plane mirrors. Two beams (red and green) are drawn for each line. The optical parts of the spectrograph are listed below:

- The transfer optics W (the blue box) to the SLED. It is detailed in Figure 11 (left) and contains the two rectangular entrance windows (4.4 mm  $\times$  31.0 mm) of the green (FeXIV) and red (FeX) beams located at the spectrograph focus.

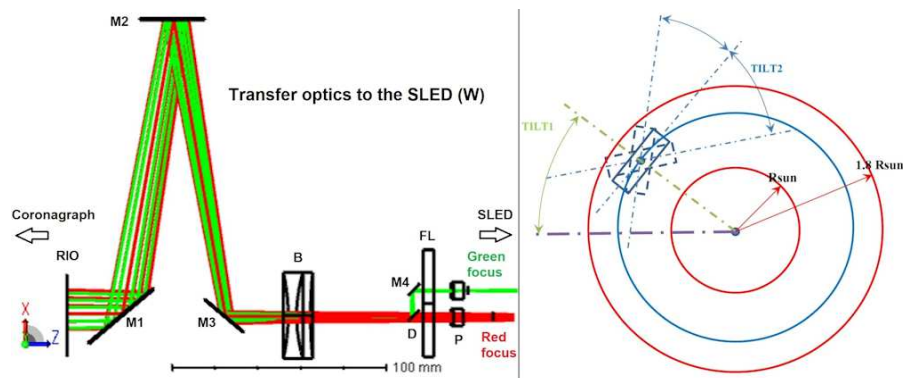


**Fig. 11** Left: transfer optics from the telescope to the SLED spectrograph in the case of the LSO Zeiss telescope. RIO = re-imaging objective (4 lenses) of the coronagraph (4.0 m secondary focus at F/20); (M1, M2, M3) = field rotator; B = Barlow (diverging doublet providing 6.0 m equivalent focus at F/30); D = dichroic mirror; FL = two field lenses; P = two compensating plates. Right: the positioning system of the 2D entrance windows; TILT1 corresponds to the axial rotation of the Zeiss mount; TILT2 comes from the rotator, as well as the adjustable distance from the limb (1.0 to 1.8 solar radii).

- The first pass (light dispersion): W, L1, M1, L2, M2, L3, L4, G (grating in pupil plane), L4, L3, M2, L2, M1, L1, M3, S (slicer).
- S = 24 channels slicer located in the spectrum (details in Figure 14). It is composed of two parts: 24 beam-splitting micro-mirrors and 24 associated beam-shifting mirrors.
- The second pass (subtractive dispersion): S (slicer), M4, M5, L1, M1, L2, M2, L3, L4, G (grating), L4, L3, M2, L2, M1, L1.
- The transfer optics to the detector: M6 (two mirrors), L5 (field lens), P (compensating plate), M7 (two mirrors), L6 (100 mm focal length objective,  $0.2 \times$  magnification, mounted on the camera).
- The Andor Zyla camera (C, 5.5 Mpixels sCMOS detector,  $2560 \times 2160$  format, 6.5 micron square pixels, USB3, Peltier and air cooled), recording the 24 channel spectra-images of the two simultaneous lines.

The optical combination of lenses (L1 and L2, L3, L4) acts as a collimator objective (2.0 m equivalent focal length) with folding mirrors (M1, M2). The grating (G) is  $62^\circ$  blazed and 79 grooves/mm ruled; the second pass on the grating subtracts the dispersion after selection of 24 channels by the slicer S. Wavelengths of observable lines in the blaze are such that  $n \times \lambda = 223531$ , where  $n$  and  $\lambda$  are respectively the order of the spectrum and wavelength ( $\text{\AA}$ ). Broad-band (100  $\text{\AA}$  FWHM) interference filters (not represented) select the order  $n$  (see Table 1).

Figure 12 does not exactly represent the final design to be easily readable. Indeed, the spectrograph will be more compact using extra folding mirrors that shown in Figure 13.

The slicer (Sayède et al., 2014) is composed of two parts: a beam-splitter of 24 micro-mirrors and a beam-shifter of 24 realigning mirrors, as shown by Figure 14. The step between the 24 micro-mirrors is 0.4 mm, providing a spectral sampling of 0.34  $\text{\AA}$  and 0.28  $\text{\AA}$ , respectively for the FeX 6374  $\text{\AA}$  and FeXIV 5302  $\text{\AA}$  coronal

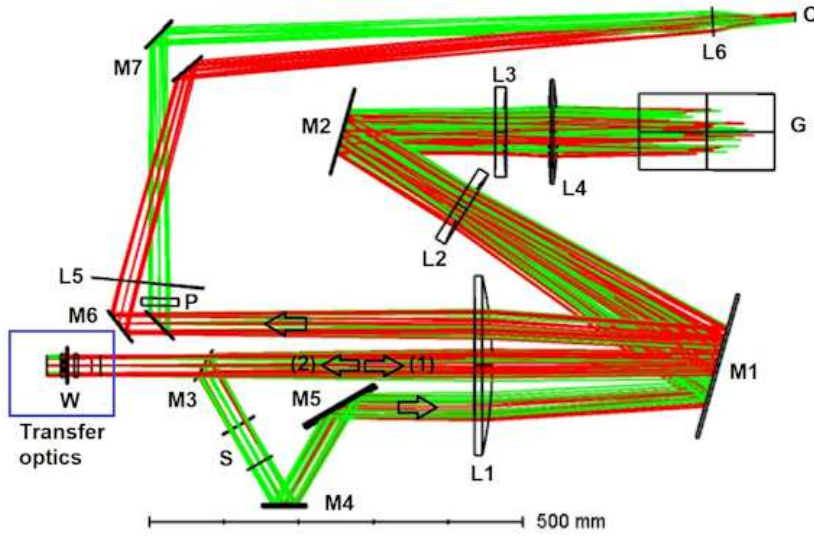


**Fig. 12** The SLED optical design; W = transfer optics containing entrance windows (see details in Figure 11); L = lenses or objectives; M = flat folding mirrors; G = grating; S = slicer; C = sCMOS camera for two simultaneous lines.

**Table 1** Capabilities of the SLED.

Wavelength (Å)	Dispersion (mm/Å)	Step (Å)	Order	Spectral resolution R
<i>Corona</i>				
6374 FeX	1.18	0.34	35	19000
5303 FeXIV	1.43	0.28	42	19000
<i>Prominences</i>				
5876 He D3	1.28	0.31	38	19000
6563 H $\alpha$	1.15	0.35	34	19000

lines (Table 1). The beam-splitter is a solid aluminum alloy component manufactured by Savimex SAS (France), with its 24 facets polished and aluminum coated (reflection range 390-900 nm). High quality polishing is crucial to avoid scattered light. The slicer is located in the spectrum. SLED's mechanical structure allows the adjustment of the 24 shifting mirrors by two rotations (around directions perpendicular to the optical axis) and one translation (along the optical axis). The adjustment's resolution is a few arc seconds for the tilts and tens of microns for the translation. Each optical path for the 24 pairs of splitting-shifting mirrors is the same length. A bench will be used to prepare the slicer, but the final alignment will be performed in the spectrograph. For each channel, the tilts allow to centre the pupil on the grating (for good uniformity and transmittance). The translation adjusts the focus of each channel and corrects the field curvature.

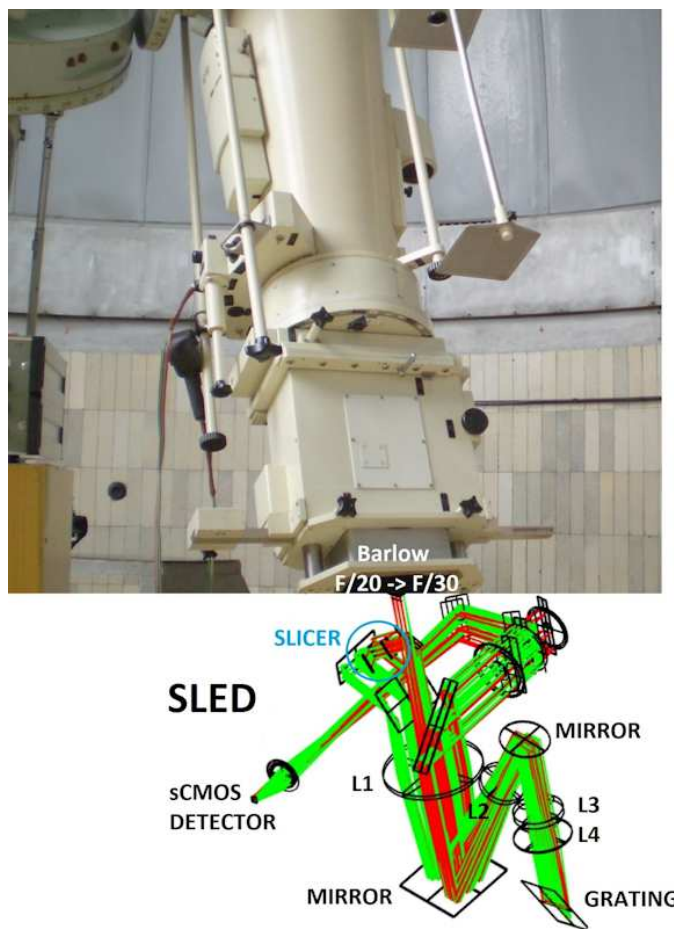


**Fig. 13** The Zeiss coronagraph at LSO (0.2 m/4.0 m) and the final design of the SLED for the green and red lines. The SLED is fed by a  $1.5 \times$  Barlow lens to work at F/30. It uses extra folding mirrors to reduce the volume and optimize the location of the gravity centre.

Focused spectra-images of both FeX and FeXIV lines, each with 24 channels, are formed simultaneously on the detector. The optical transmittance of the SLED for these lines is 0.25, as shown by Figure 15, and is greater than 0.2 over the entire range 5000 - 7000 Å. There is almost no transmission above 8000 Å, which means that IR lines cannot be observed. For instance, the IR lines (FeXI 7892 Å and FeXIII 10747 Å) planned to be observed by the future Visible Emission Line Coronagraph (VELC) onboard the Indian Aditya-L1 mission (Raj Kumar et al. (2018), Raghavendra Prasad et al. (2017)) are not accessible to the SLED, but coordinated campaigns could be organized in the FeXIV 5303 Å line with both instruments. The sCMOS camera has a quantum efficiency greater than 0.5 over the wavelength range 4250 - 8000 Å and the overall transmittance of the SLED is reported in Figure 15.

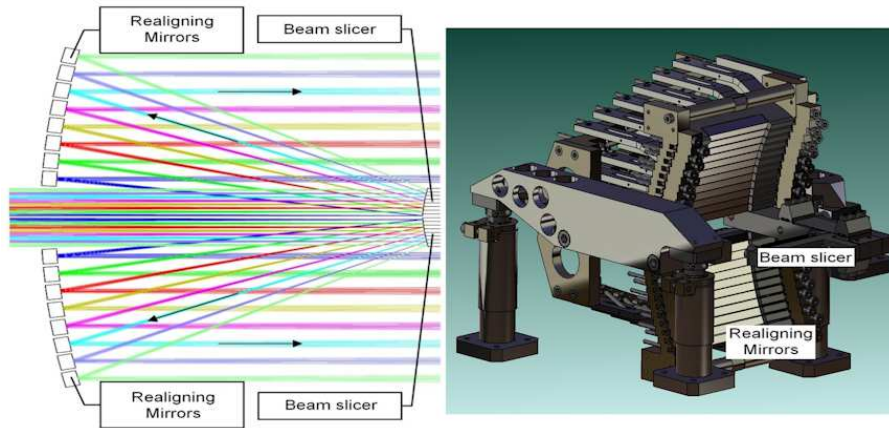


**Fig. 14** The slicer S is the core of the SLED. It is composed of 24 beam-splitting micro-mirrors (0.4 mm step) and 24 beam-shifting mirrors (the figure does not show the full number of mirrors).

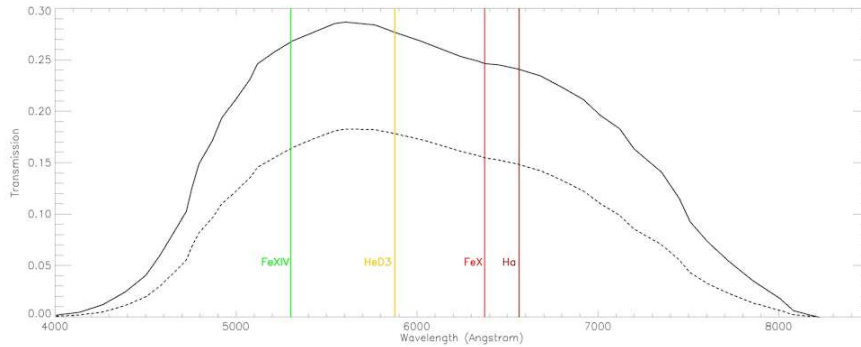


**Fig. 15** SLED transmission curves as a function of wavelength ( $\text{\AA}$ ). Solid line: optical transmittance; dashed line: overall transmittance including the detector. Coronal lines (FeX and FeXIV) and prominence lines (He D3 and H $\alpha$ ) are indicated.

## 6 Conclusion

The Solar Line Emission Dopplerometer (SLED) is a state-of-the-art and innovative instrument for investigating the dynamics of coronal structures in the forbidden lines of FeX and FeXIV using high altitude coronagraphs. Dopplergrams ( $150'' \times 1000''$  FOV,  $2.1''$  pixel sampling), providing the line-of-sight velocity, will be produced at high cadence (1 Hz). This original feature will allow us to observe plasma motions during fast-evolving events such as flares or CMEs driving space weather phenomena, and also high-frequency oscillations and waves implied in coronal heating. Full line profiles ( $0.28 \text{ \AA}$  resolution) will be available for all pixels of the FOV. The SLED will complement SDO/AIA (EUV intensities of hot lines) and ground-based coronal imagers such as SECIS. It uses an imaging spectroscopy technique which is faster than most tunable filters and narrow slit spectrographs. The SLED will supplement



spectroscopic instruments operating mainly in IR lines, such as CoMP or the future VELC instrument onboard Aditya-L1 (Raj Kumar et al., 2018). The Multi-slit Solar Explorer (MUSE) project (De Pontieu et al., 2020) is another approach for EUV spectroscopy in space. SLED will follow the coronal activity of cycle 25 at Lomnický Štít Observatory, but will also be tested at Białków to study the dynamics of prominences. As it is a portable instrument, it could also be deployed to observe total solar eclipses, such as the event of 8 April 2024 visible from North America.

**Acknowledgements** The authors thank the referee for helpful comments and suggestions. We are grateful for financial support to the Institut National des Sciences de l'Univers (INSU/CNRS), the University of Wrocław, the UK Science and Technology Facilities Council (STFC), the Leverhulme Trust via grant RPG-2019-371, and Queen's University Belfast. J.R. acknowledges support by the Science Grant Agency project VEGA 2/0048/20 (Slovakia). P. Rudawy were supported by the National Science Centre in Poland, under grant No. UMO-2015/17/B/ST9/02073.

## References

- Ambróz J, Radziszewski K, Rudawy P, Rybák J, Phillips KJH (2010) The SECIS instrument on the Lomnický Peak Observatory. *Contributions of the Astronomical Observatory Skalnaté Pleso* 40(1):5–18, 1004. 3454
- Boe B, Habbal S, Druckmüller M, Landi E, Kourkchi E, Ding A, Starha P, Hutton J (2018) The First Empirical Determination of the Fe<sup>10+</sup> and Fe<sup>13+</sup> Freeze-in Distances in the Solar Corona. *Astrophys. J.* 859(2):155, DOI 10.3847/1538-4357/aabfb7
- Brueckner GE, Howard RA, Koomen MJ, Korendyke CM, Michels DJ, Moses JD, Socker DG, Dere KP, Lamy PL, Llebaria A, Bout MV, Schwenn R, Simnett GM, Bedford DK, Eyles CJ (1995) The Large Angle Spectroscopic Coronagraph (LASCO). *Solar Phys.* 162(1-2):357–402, DOI 10.1007/BF00733434
- Chisholm JH, James JC (1964) Radar Evidence of Solar Wind and Coronal Mass Motions. *Astrophys. J.* 140:377, DOI 10.1086/147928
- De Pontieu B, Martínez-Sykora J, Testa P, Winebarger AR, Daw A, Hansteen V, Cheung MCM, Antolin P (2020) The Multi-slit Approach to Coronal Spectroscopy with the Multi-slit Solar Explorer (MUSE). *Astrophys. J.* 888(1):3, DOI 10.3847/1538-4357/ab5b03, 1909.08818
- Desai JN, Chandrasekhar T, Angreji PD (1982) Doppler shift measurements on the green coronal line - Evidence for largescale macroscopic mass motion. *Journal of Astrophysics and Astronomy* 3:69–77, DOI 10.1007/BF02714564
- Habbal SR, Cooper J, Daw A, Ding A, Druckmüller M, Esser R, Johnson J, Morgan H (2011) Exploring the Physics of the Corona with Total Solar Eclipse Observations. arXiv e-prints arXiv:1108.2323, 1108.2323
- James JC (1970) Some Observed Characteristics of Solar Radar Echoes and Their Implications. *Solar Phys.* 12(1):143–162, DOI 10.1007/BF02276574
- Klimchuk JA (2006) On Solving the Coronal Heating Problem. *Solar Phys.* 234(1):41–77, DOI 10.1007/s11207-006-0055-z, astro-ph/0511841

- Lee JO, Lee KS, Seough J, Cho KS (2021) Comparison of LOS Doppler Velocities and Non-thermal Line Widths in the Off-limb Solar Corona Measured Simultaneously by CoMP and Ninode/EIS. *Journal of Korean Astronomical Society* 54:49–60
- Lexa J (1963) New coronagraph of the Astronomical Observatory of the Slovak Academy of Sciences at Skalnaté Pleso. *Bulletin of the Astronomical Institutes of Czechoslovakia* 14:107
- Livingston W, Harvey J (1982) Preliminary results from eclipse coronal velocity observations. *Proceedings of the Indian National Science Academy Part A* 48:18–28
- Livingston W, Harvey J, Doe LA, Gillespie B, Ladd G (1980) The Kitt-Peak Coronal Velocity Experiment. *Bulletin of the Astronomical Society of India* 8:43
- Mein P (1977) Multi-channel subtractive spectrograph and filament observations. *Solar Phys.* 54(1):45–51, DOI 10.1007/BF00146423
- Mein P, Malherbe JM, Sayède F, Rudawy P, Phillips KJH, Keenan FP (2021) Four Decades of Advances from MSDP to S4I and SLED Imaging Spectrometers. *Solar Phys.* 296(2):30, DOI 10.1007/s11207-021-01766-9, 2101.03918
- Mierla M, Schwenn R, Teriaca L, Stenborg G, Podlipnik B (2008) Analysis of the Fe X and Fe XIV line width in the solar corona using LASCO-C1 spectral data. *Astron. Astrophys.* 480(2):509–514, DOI 10.1051/0004-6361:20078329, 0903.0496
- Minarovjech M, Rušin V, Rybanský M, Sakurai T, Ichimoto K (2003) Oscillations in the Coronal Green-Line Intensity Observed at Lominický Štít and Norikura Nearly Simultaneously. *Solar Phys.* 213(2):269–290, DOI 10.1023/A:1023938732756
- Morton RJ, Tomczyk S, Pinto RF (2016) A Global View of Velocity Fluctuations in the Corona below  $1.3 R_{\odot}$  with CoMP. *Astrophys. J.* 828(2):89, DOI 10.3847/0004-637X/828/2/89, 1608.01831
- Phillips KJH, Read PD, Gallagher PT, Keenan FP, Rudawy P, Rompolt B, Berlicki A, Buczylo A, Diego F, Barnsley R, Smartt RN, Pasachoff JM, Babcock BA (2000) SECIS: The Solar Eclipse Coronal Eclipse Imaging System. *Solar Phys.* 193:259–271, DOI 10.1023/A:1005274827585
- Pomoell J, Poedts S (2018) EUHFORIA: European heliospheric forecasting information asset. *Journal of Space Weather and Space Climate* 8:A35, DOI 10.1051/swsc/2018020
- Raghavendra Prasad B, Banerjee D, Singh J, Nagabhushana S, Kumar A, Kamath PU, Kathiravan S, Venkata S, Rajkumar N, Natarajan V, Juneja M, Somu P, Pant V, Shaji N, Sankarsubramanian K, Patra A, Venkateswaran R, Adoni AA, Narendra S, Haridas TR, Mathew SK, Mohan Krishna R, Amareswari K, Jaiswal B (2017) Visible Emission Line Coronagraph on Aditya-L1. *Current Science* 113(4):613
- Raj Kumar N, Raghavendra Prasad B, Singh J, Venkata S (2018) Optical design of visible emission line coronagraph on Indian space solar mission Aditya-L1. *Experimental Astronomy* 45(2):219–229, DOI 10.1007/s10686-017-9569-7
- Reale F (2010) Coronal Loops: Observations and Modeling of Confined Plasma. *Living Reviews in Solar Physics* 7(1):5, DOI 10.12942/lrsp-2010-5, 1010.5927
- Rochus P, Auchère F, Berghmans D, Harra L, Schmutz W, Schühle U, Addison P, Appourchaux T, Aznar Cuadrado R, Baker D, Barbay J, Bates D, BenMoussa A, Bergmann M, Beurthe C, Borgo B, Bonte K, Bouzit M, Bradley L, Büchel V, Buchlin E, Büchner J, Cabé F, Cadiergues L, Chaigneau M, Chares B, Choque

- Cortez C, Coker P, Condamin M, Coumar S, Curdt W, Cutler J, Davies D, Davison G, Defise JM, Del Zanna G, Delmotte F, Delouille V, Dolla L, Dumesnil C, Dürig F, Enge R, François S, Fourmond JJ, Gillis JM, Giordanengo B, Gissot S, Green LM, Guerreiro N, Guilbaud A, Gyo M, Haberreiter M, Hafiz A, Hailey M, Halain JP, Hansotte J, Hecquet C, Heerlein K, Hellin ML, Hemsley S, Hermans A, Hervier V, Hochedez JF, Houbrechts Y, Ihsan K, Jacques L, Jérôme A, Jones J, Kahle M, Kennedy T, Klaproth M, Kolleck M, Koller S, Kotsialos E, Kraaikamp E, Langer P, Lawrenson A, Le Clech' JC, Lenaerts C, Liebecq S, Linder D, Long DM, Mampaey B, Markiewicz-Innes D, Marquet B, Marsch E, Matthews S, Mazy E, Mazzoli A, Meining S, Meltchakov E, Mercier R, Meyer S, Monecke M, Monfort F, Morinaud G, Moron F, Mountney L, Müller R, Nicula B, Parenti S, Peter H, Pfiffner D, Philippon A, Phillips I, Plessier JY, Pyllyser E, Rabecki F, Ravet-Krill MF, Rebellato J, Renotte E, Rodriguez L, Roose S, Rosin J, Rossi L, Roth P, Rouesnel F, Roulliay M, Rousseau A, Ruane K, Scanlan J, Schlatter P, Seaton DB, Silliman K, Smit S, Smith PJ, Solanki SK, Spescha M, Spencer A, Stegen K, Stockman Y, Szewc N, Tamiatto C, Tandy J, Teriaca L, Theobald C, Tychon I, van Driel-Gesztelyi L, Verbeeck C, Vial JC, Werner S, West MJ, Westwood D, Wiegelmann T, Willis G, Winter B, Zerr A, Zhang X, Zhukov AN (2020) The Solar Orbiter EUVI instrument: The Extreme Ultraviolet Imager. *Astron. Astrophys.*642:A8, DOI 10.1051/0004-6361/201936663
- Roudier T, Malherbe JM, Moity J, Rondi S, Mein P, Coutard C (2006) Sub arcsec evolution of solar magnetic fields. *Astron. Astrophys.*455(3):1091–1098, DOI 10.1051/0004-6361:20064963
- Rudawy P, Phillips KJH, Gallagher PT, Williams DR, Rompolt B, Keenan FP (2004) Search for 1–10 Hz modulations in coronal emission with SECIS during the August 11, 1999 eclipse. *Astron. Astrophys.*416:1179–1186, DOI 10.1051/0004-6361:20031737
- Rudawy P, Phillips KJH, Buczyłko A, Williams DR, Keenan FP (2010) Search for Rapid Changes in the Visible-Light Corona during the 21 June 2001 Total Solar Eclipse. *Solar Phys.*267(2):305–327, DOI 10.1007/s11207-010-9647-8, 1009.5205
- Rudawy P, Radziszewski K, Berlicki A, Phillips KJH, Jess DB, Keys PH, Keenan FP (2019) A Search for High-Frequency Coronal Brightness Variations in the 21 August 2017 Total Solar Eclipse. *Solar Phys.*294(4):48, DOI 10.1007/s11207-019-1428-4, 1903.06076
- Sakurai T, Ichimoto K, Raju KP, Singh J (2002) Spectroscopic Observation of Coronal Waves. *Solar Phys.*209(2):265–286, DOI 10.1023/A:1021297313448
- Sayède F, Mein P, Malherbe JM, Amans JP, Crussaire D, Lecocguen R (2014) The S4I prototype, a beam-slicer dedicated to the new generation Multichannel Subtractive Double Pass for EST imaging spectropolarimetry. In: Ramsay SK, McLean IS, Takami H (eds) Ground-based and Airborne Instrumentation for Astronomy V, Society of Photo-Optical Instrumentation Engineers (SPIE) Conference Series, vol 9147, p 91476F, DOI 10.1117/12.2054947
- Schmieder B, Tian H, Kucera T, López Ariste A, Mein N, Mein P, Dalmasse K, Golub L (2014) Open questions on prominences from coordinated observations by IRIS, Hinode, SDO/AIA, THEMIS, and the Meudon/MSDP. *Astron. Astro-*

- phys.*569:A85, DOI 10.1051/0004-6361/201423922, 1407.3171
- Schrijver CJ, Beer J, Baltensperger U, Cliver EW, Güdel M, Hudson HS, McCracken KG, Osten RA, Peter T, Soderblom DR, Usoskin IG, Wolff EW (2012) Estimating the frequency of extremely energetic solar events, based on solar, stellar, lunar, and terrestrial records. *Journal of Geophysical Research (Space Physics)* 117(A8):A08103, DOI 10.1029/2012JA017706, 1206.4889
- Shibata K, Magara T (2011) Solar Flares: Magnetohydrodynamic Processes. *Living Reviews in Solar Physics* 8(1):6, DOI 10.12942/lrsp-2011-6
- Singh J, Sakurai T, Ichimoto K, Suematsu Y, Takeda A (2002) Spectroscopic Studies of the Solar Corona II. Properties of Green and Red Emission Lines in Open and Closed Coronal Structures. *Pub. Astron. Soc. Japan*54:793–806, DOI 10.1093/pasj/54.5.793
- Tomczyk S, McIntosh SW, Keil SL, Judge PG, Schad T, Seeley DH, Edmondson J (2007) Alfvén Waves in the Solar Corona. *Science* 317(5842):1192, DOI 10.1126/science.1143304
- Tomczyk S, Card GL, Darnell T, Elmore DF, Lull R, Nelson PG, Stenander KV, Burkepile J, Casini R, Judge PG (2008) An Instrument to Measure Coronal Emission Line Polarization. *Solar Phys.*247(2):411–428, DOI 10.1007/s11207-007-9103-6

## A Online material

MPEG4 movie showing a simulation of the 24 channel spectral images of the SLED for the coronal green line (FeXIV 5303 Å, top) and red line (FeX 6374 Å, middle). Three rectangular structures have been chosen (centre, left and right of the FOV) with LOS velocities continuously varying from  $-100 \text{ km s}^{-1}$  to  $+100 \text{ km s}^{-1}$  (intensity I and velocity V at the right of the display, intensity in green with blueshift and redshift).

The bottom panel shows the corresponding line profiles (left: green line; right: red line), for structures located in the centre and both sides of the FOV. The wavelength (Å) is centred. The spectral range (6.5 and 8.0 Å respectively for the green and red line) is constant across the FOV but shifts according to the x-position. Velocities up to  $\pm 75 \text{ km s}^{-1}$  can be measured in any point of the FOV, and much more near the centre.